Adipocyte Spatial Distributions in Bone Marrow: Implications for Skeletal Dosimetry Models

Amish P. Shah, MS[1]; Phillip W. Patton, PhD[2]; Didier A. Rajon, MS[3]; and Wesley E. Bolch, PhD[1,3]

[1]Department of Biomedical Engineering, University of Florida, Gainesville, Florida; [2]Department of Health Physics, University of Nevada–Las Vegas, Las Vegas, Nevada; and [3]Department of Nuclear and Radiological Engineering, University of Florida, Gainesville, Florida

Few studies have been conducted to quantify the spatial distributions of adipocytes in the marrow cavities of trabecular bone. Nevertheless, such data are needed for the development of 3-dimensional (3D) voxel skeletal models where marrow cellularity is explicitly considered as a model parameter for dose assessment. In this investigation, bone marrow biopsies of the anterior iliac crest were examined to determine the size distribution of adipocyte cell clusters, the percentage of perimeter coverage of trabecular surfaces, and the presence or absence of adipocyte density gradients in the marrow space, all as a function of the biopsy marrow cellularity (5%–95%). **Methods:** Biopsy slides from 42 patients were selected as designated by the hematopathologist as either normocellular or with no evidence of disease. Still-frame video image captures were made of 1–3 regions of interest per biopsy specimen, with subsequent image analysis of adipocyte spatial characteristics performed via a user-written MATLAB routine. **Results:** A predictable shift was found in cluster size with decreasing marrow cellularity from single adipocytes to clusters of ≥3 cells; the percentage of 2-cell clusters remained relatively constant with changing cellularity. Also, a nonlinear increase in trabeculae perimeter coverage was found with increasing fat tissue fraction at marrow cellularities between 50% and 80%. Finally, it was demonstrated that only in the range of 20%–50% marrow cellularity was a slight gradient in adipocyte concentration indicated with adipocytes localized preferentially toward the trabecular surfaces. **Conclusion:** Electron transport simulations were conducted in 4 different 3D voxel models of trabecular bone for sources localized in the active marrow (TAM), bone volume (TBV), bone endosteum (TBE), and bone surfaces (TBS). Voxel model simulations demonstrated that absorbed fractions to active marrow given by the ICRP 30 model (MIRDOSE2) are exceedingly conservative for both TBV and TBS sources, except in the case of high-energy particles (>500 keV) at high values of marrow cellularity (>70%). Values of both ϕ(TAM←TBV) and ϕ(TAM←TBS) given by the Eckerman and Stabin model (MIRDOSE3) were shown to be reasonably consistent with 3D voxel model simulations at the reference cellularity of 25%, except in the case of low-energy emitters (<100 keV) on the bone surfaces.
Key Words: active (red) marrow; adipocyte; skeletal dosimetry; nuclear magnetic resonance microscopy; marrow dosimetry
J Nucl Med 2003; 44:774–783

The need for improved patient specificity of skeletal dosimetry models is widely recognized in the field of radionuclide therapy. Patient specificity in the absorbed dose to active (red) marrow requires separate assessments of the amount of radioactivity taken up within skeletal tissues of the patient and the absorbed dose per particle emission (S value), considering the patient's internal skeletal structure (normal, osteopenic, or osteoporotic trabecular lattice), external skeletal structure (size of the spongiosa and bone cortex), and marrow composition (cellularity). Extensive efforts have been made in patient-specific assessments of activity uptake in active marrow, including estimation of marrow activity concentration as a function of the peripheral blood concentration (*1*) or via direct imaging of skeletal regions with high active-marrow content (*2–6*). Little research, however, has been focused on improving the patient specificity of radionuclide S values.

Considerations of patient marrow cellularity may be an important factor in improving correlations between marrow dose and hematopoietic toxicity. To this end, chemical-shift MRI techniques have been proposed whereby marrow cellularity can be assessed in vivo (*7,8*). Skeletal dosimetry models can then be applied in which marrow cellularity is not simply a fixed constant per skeletal site but is permitted to vary continuously as measured in the patient, allowing for potential changes due to damage from prior chemotherapy or other treatments (*9*). Although individual patient measurements of marrow cellularity would be ideal, economic and practical constraints might limit this approach. In these cases, clinical implementation of MR-based cellularity adjustments of S values could be based on standard cellularity values representing mean values for different patient and

population groups (e.g., those receiving prior chemotherapy, women in their 70s, and so forth).

Rozman et al. (10) conducted one of the first comprehensive studies of human marrow adipocytes. In that study, 20 biopsy specimens taken from the anterior iliac crest were examined using stereologic methods. Adipocyte diameters were found to be normally distributed with mean diameters that increased linearly with increasing marrow fat fraction: ~50-μm diameter at 15% fat fraction (cellularity, 85%) and ~65-μm diameter at 50% fat fraction (cellularity, 50%). Increases in marrow fat fraction were found to depend on both increases in the size of individual adipocytes and increases in the number of adipocytes within the marrow cavities. Adipocyte size accounted for 66.2% of the fat tissue fraction, whereas both size and cell number explained 97.2% of the fat tissue fraction. The group found similar results for biopsies of abnormal marrow (11).

Allen et al. (12) later confirmed many of the observations made by Rozman et al. (10,11) through observations of marrow in human ribs. These authors, however, found that the adipocyte diameters were better characterized as proportional to the cube root of the fat tissue fraction, thus predicting mean diameters of 49, 64, and 75 μm at fat tissue fractions of 20%, 50%, and 70%, respectively. Additionally, these authors quantified frequency distributions of distances between individual adipocytes and the nearest trabecular bone surface. Although many observations were consistent with a uniform distribution of adipocytes in the marrow cavities, some specimens displayed a propensity for adipocyte localization closer to the trabecular surfaces, with lower concentrations interior to the marrow cavities. This formation of a "first fat layer" (50% coverage of bone surfaces by definition) can have important consequences for active marrow dose assessments by low-energy particle emissions either within the volume or on the surfaces of the bone trabeculae.

The purpose of this study was to provide the experimental data needed to implement histologically realistic distributions of marrow adipocytes within 3-dimensional (3D) nuclear magnetic resonance (NMR)-based voxel models of trabecular bone. In these models, image segmentation techniques are used to separate bone voxels from marrow space voxels in the 3D skeletal image. The marrow voxels are then further differentiated into voxels of active (red) marrow and inactive (yellow) marrow, the latter representing adipocytes and their cell clusters. Specific investigations of this study include the characterization of adipocyte cell cluster sizes, the percentage of trabecular bone surfaces (TBS) covered by adipocytes, and the changes in local marrow cellularity as a function of distance interior to the marrow cavity.

MATERIALS AND METHODS

Selection of Bone Marrow Biopsy Specimens

Bone marrow biopsy slides, archived from earlier examinations of the anterior iliac crest, were obtained from the Hematopathology Section, Department of Pathology, at the University of Florida Shands Hospital. Selection criteria were established to identify specimens representing normal spatial distributions of adipocytes within their marrow cavities. Biopsies designated by the hematopathologist as either normocellular or with no evidence of disease were entered into the study. The former designation indicates biopsies that fall within accepted age-dependent ranges of cellularity for disease-free individuals. The latter designation excluded specimens showing either inadequate cell maturation or displaying abnormalities such as tumors, myelodysplasia, neoplasia, or lymphoma. Biopsies with normal pathology, but which contained some areas of hypercellularity or hypocellularity, were also included. The study population included 42 patients in both diagnostic categories: 11 females with normocellular marrow (age, 21–71 y), 10 females with no evidence of disease (age, 24–69 y), 9 males with normocellular marrow (age, 2–63 y), and 12 males with no evidence of disease (age, 7–55 y).

Image Acquisition and Processing

Image capture was conducted using a Digital Photo Camera (model DKC-5000; Sony Corp., San Diego, CA) attached to an Eclipse E1000 optical microscope (Nikon, Melville, NY) in the University of Florida hematopathology laboratory. Each biopsy sample was first examined for regions of interest (ROIs) that included clear delineations of active marrow, adipose tissue, and trabecular bone. Areas of exclusion included regions of blood spillage, incomplete or irregular biopsies, or abundance of trabecular or cortical bone either torn or grouped from the extraction process. Once acceptable ROIs were identified, the images were still-framed, recorded, and saved in JPEG format for subsequent use with a user-written MATLAB (The MathWorks, Inc., Natick, MA) routine for spatial measurements (adipocyte cluster sizes, trabeculae perimeters, and so forth). Distance measurements were calibrated against reference markings on a stage micrometer (Fisher Scientific, Pittsburgh, PA) at equivalent magnification (4× or 10×). Marrow cellularity for each biopsy specimen was determined, as in clinical practice, via visual inspection using a chart of reference biopsy images indexed at cellularity increments of 10%. Marrow cellularities within selected ROIs were thus assigned to the nearest 5% (5%, 10%,... 90%, 95%) via reference image interpolation. Between 1 and 3 specimens, each with 2 or 3 ROIs per specimen, were examined at each value of cellularity between 5% and 95%. Representative images at 30% and 80% are shown in Figure 1.

Frequency Distribution of Adipocyte Cluster Size (Study 1)

In this first study, image ROIs were reviewed to measure the frequency distribution of adipocyte cluster size interior to the
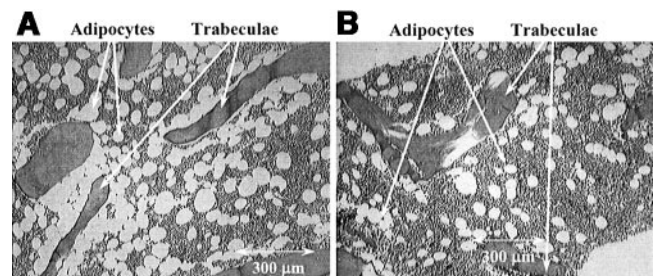
FIGURE 1. Video capture images of 2 bone marrow biopsy specimens. (A) Marrow at 30% cellularity. (B) Marrow at 80% cellularity.

marrow cavities as a function of the marrow cellularity. Cluster sizes ranged from single isolated cells to groupings of up to 9 cells. Clusters of ≥10 cells were difficult to quantify with respect to cell number and were thus assigned to a single category of 10 or more cells. For cellularities ≤30% (fat fractions, ≥70%), adipocyte cluster size became visually indeterminate in the marrow spaces.

Percentage of Trabecular Surfaces Covered by Adipocytes (Study 2)

In this second study, measurements were made to quantify the presence and extent of the first fat layer on the surfaces of the bone trabeculae. For each patient image, a MATLAB routine was first used to measure the total perimeter for all trabeculae visible within the ROI (2.03 μm/pixel at 10× magnification). Next, a reduced trabeculae perimeter was estimated that contained only those sections of the trabecular surfaces that were in immediate contact with surface adipocytes (single cells or cell clusters). Ratios of the adipocyte-covered perimeter to the total trabeculae perimeter were calculated and then indexed to the marrow cellularity of the biopsy specimen.

Marrow Cellularity as Function of Distance from Trabecular Surfaces (Study 3)

A third study was conducted to quantify any spatial preference for adipocyte cluster formation within the marrow cavities at differing marrow cellularities. In particular, the study sought to determine if adipocyte clusters were uniformly distributed in the marrow cavities or preferentially distributed either toward or away from the trabecular surfaces. For each image ROI, contours were drawn at distances of 100, 200, and 300 μm from all trabecular surfaces. Next, visual inspections of marrow cellularity were made within each marrow region (0–100, 100–200, 200–300, and >300 μm from the bone–marrow interface). Values of local cellularity and their gradients were then indexed to the global cellularity measured across the entire image ROI.

Bone Sample Acquisition and NMR Microscopy

In this study, previously segmented and filtered NMR microscopy images of the femoral head and humeral epiphysis of a 51-y-old male subject and a 82-y-old female subject were used in the simulation of adipocyte spatial distributions and the resulting β-particle (electron) dosimetry of the active marrow. Details regarding sample harvesting, sample preparation, and NMR microscopy image acquisition and processing are given in Bolch et al. (9) and in Patton et al. (13). The images were acquired on a 20-cm wide-bore Avance imaging spectrometer (Bruker Medical, Karlsruhe, Germany) operated at a 200-MHz proton resonance (4.7-T magnetic field strength) using a 35-mm-diameter quadrature birdcage coil of length 4.5 cm. A conventional 3D spin-echo pulse sequence was used to obtain fully 3D images of the sample at a spatial resolution of 88 × 88 × 88 μm. Voxels in the 3D binary image were assigned to either the bone trabeculae or to the bone marrow. Bone endosteum was further defined as that portion of marrow surface voxels 10 mm from the surface of an adjacent bone voxel. The residual voxel volumes were assigned to bone marrow, thus creating a 10-μm boundary of endosteum separating the osseous tissues of the bone trabeculae and the tissues of the marrow cavity.

### Methods for Adipocyte Introduction Within Voxel Models of Trabecular Bone

In the previous study by Bolch et al. (9), marrow voxels in the binary 3D NMR images were partitioned into those belonging to either trabecular active marrow (TAM) or trabecular inactive marrow (TIM), the later identifying marrow adipose tissue. Regions of TIM were modeled in Bolch et al. as randomly positioned 3-voxel groupings placed uniformly within the marrow cavities (3-Voxel method). In this study, 2 additional methods are explored: RANDOM and DEFINED. The former randomly tags marrow voxels in the original binary image as adipose tissue 1 voxel at a time. In the DEFINED method, the spatial arrangement of the TIM voxels is forced to conform to measurements made on the biopsy specimens (studies 1–3) (assuming no skeletal-site dependence on their spatial distribution). First, clusters of marrow voxels on the trabecular surfaces are tagged as TIM according to both the cluster size distribution of study 1 and the percentage of perimeter coverage of study 2. It is assumed that values of percentage of area coverage in the 3D bone images are equivalent to measurements of percentage of perimeter coverage in the 2-dimensional (2D) biopsy images. Second, clusters of TIM voxels in the interior of the marrow cavities are created in a manner consistent with the cluster size distribution of study 1 and any cellularity gradients observed in study 3. Additional clusters are created until an overall targeted marrow cellularity is achieved. To verify the accuracy of the algorithms of the DEFINED method, 2D slices were extracted through the resulting 3D image and values of cluster size distribution and percentage of perimeter coverage of trabecular surfaces were tabulated and compared with the measured values of studies 1 and 2. Figure 2 shows representative 2D slices through the femoral head of the 51-y-old man at 3 values of marrow cellularity via the DEFINED method. Final 3D images of trabecular bone, with both active and inactive marrow regions present, were then coupled to the EGS4 radiation transport code. Particle transport (10,000 histories) was initiated for electron sources (10 keV to 4 MeV) originating in the TAM, trabecular bone endosteum (TBE), TBS, or trabecular bone volume (TBV). Particle histories of 10^5 were simulated so that errors on the absorbed fraction to the TAM were held to <1% in each case.

RESULTS

Frequency Distribution of Adipocyte Cluster Size (Study 1)

Figure 3 displays the relative number of adipocyte clusters as functions of both the cluster cell size and the marrow
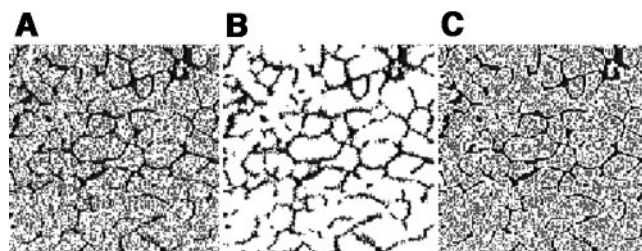

FIGURE 2. Representative slices from 3D segmented NMR images of 51-y-old male femoral head. Black, white, and gray pixels represent bone trabeculae, active marrow, and adipose tissue, respectively, with the latter implemented using the DEFINED method of voxel tagging. Images are shown for 60% marrow cellularity (A), 60% cellularity showing only bone surface adipose voxels (B), and 60% cellularity showing only marrow space adipose voxels (C). Scale of each panel is 17.3 mm on edge.
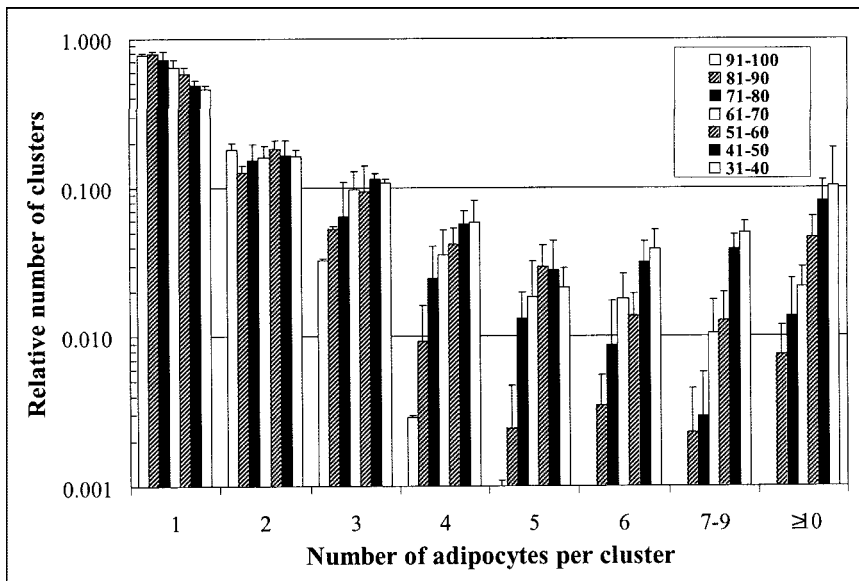
FIGURE 3. Frequency distribution of adipocyte cluster cell size as function of marrow cellularity from 30% to 100%.

cellularity of the biopsy sample. At extremely high marrow cellularities (>90%), adipocytes are found primarily as isolated cells (~0.78) or as clusters of 2 or 3 cells (~0.18 and ~0.03, respectively). As the cellularity of the bone marrow decreases, the relative number of single adipocytes decreases accordingly (down to ~0.46 at 30%–40% marrow cellularity), whereas the relative number of 2-cell clusters remains fairly constant at between 0.13 and 0.18 across all cellularities considered. Concurrently, increases are noted in the relative proportions of multicell clusters with decreasing cellularity at each cluster size of ≥3 cells. These frequency distributions were constructed with approximately 4 or 5 biopsy subjects per 10% marrow cellularity interval, with the 30%–40% grouping having 3 subjects and the 90%–100% grouping having only 2 subjects. At cellularities of <30%, the density of adipocytes was such that individual cell clusters could not be identified.

Figure 4 gives a comparison of the measured cluster size distributions with corresponding distributions of voxel cluster sizes in the 3D NMR images for the 51-y-old male femoral head as implemented via the DEFINED and RANDOM methods of marrow voxel tagging. At high values of marrow cellularity (90%–100% in Fig. 4A), the DEFINED method is shown to provide a slightly better depiction of the measured distribution than a simple random tagging of voxels in the marrow spaces, particularly for the larger cell clusters (≥6 cells). As the cellularity of the bone marrow decreases (30%–40% in Fig. 4B), the DEFINED and RANDOM methods of marrow voxel tagging yield comparable distributions, with both giving fairly good approximations to the measured distributions of adipocyte cluster sizes. In general, the DEFINED method of voxel tagging was shown to be slightly superior to the RANDOM distribution at marrow cellularities of >50%. Both methods were comparable at
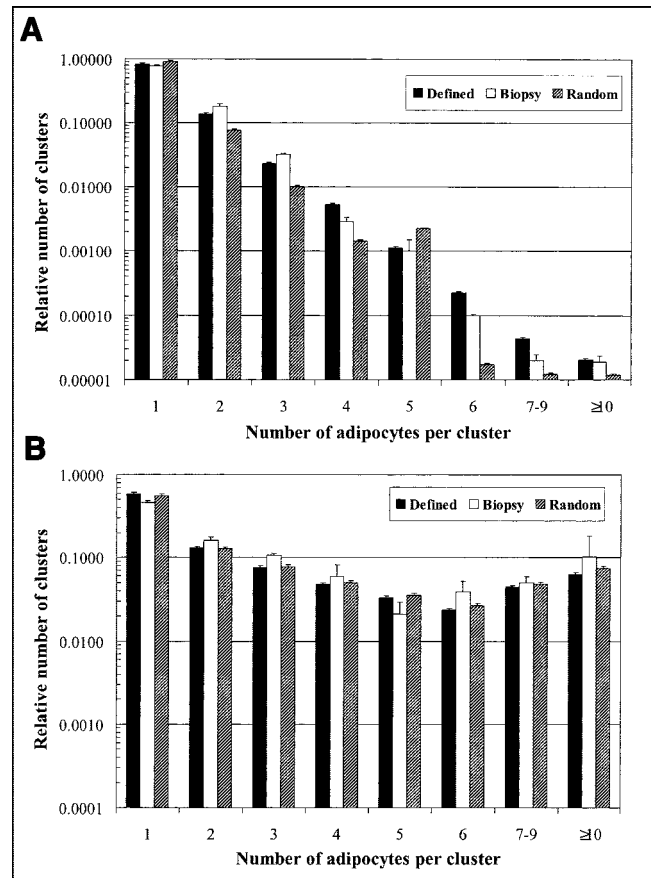
FIGURE 4. Comparison of relative number of adipocytes per cluster within marrow cavity as measured in marrow biopsies (□) and as simulated in NMR microscopy images using DEFINED (■) and RANDOM (▨) methods of voxel tagging. Comparisons are made at marrow cellularities of 90%–100% (A) and 30%–40% (B).

cellularities of <50%, indicating that adipocytes are positioned randomly in the marrow spaces.

## Percentage of Trabecular Surfaces Covered by Adipocytes (Study 2)

Figure 5 displays measured values (closed circles) of the percentage of bone trabeculae perimeter that is in contact with marrow adipocytes as a function of the marrow cellularity. At a marrow cellularity of 95%, ~8% of the trabecular perimeter in the biopsy images is covered by adipocytes. This perimeter coverage increases to ~27% as the marrow cellularity drops to 65%, after which the rate of perimeter coverage is noted to increase more rapidly until ~55% of the perimeter is covered by adipocytes at a marrow cellularity of 45%. The rate of coverage then decreases slightly as marrow cellularity further declines (and the fat fraction approaches 100%). For comparison, the percentage of trabecular surfaces covered by adipose voxels in the 3D NMR images is shown using the RANDOM and the DEFINED methods (the latter designed to reproduce measured values of perimeter coverage). Not surprisingly, the RANDOM method of voxel tagging yields a uniformly increasing percentage of trabecular perimeter coverage by adipose voxels with decreasing marrow cellularity. Deviations from this RANDOM method are noted in the marrow cellularity range of 50%–80%. The measurements are consistent with the initial appearance of a first fat layer on the trabecular surfaces at marrow cellularities at and below ~65% (fat fractions, ≥35%). The first fat layer (50% perimeter coverage) is thus fully established at a cellularity of ~45%.

Marrow Cellularity as Function of Distance from Trabecular Surfaces (Study 3)

In this study, the radial distribution of marrow cellularity as a function of distance into the marrow space is assessed.
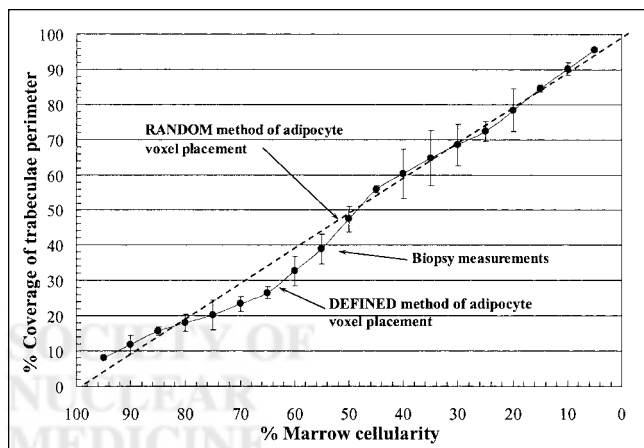
FIGURE 5. Percentage of bone trabeculae perimeter that is in immediate contact with marrow adipocytes (● – biopsy measurements). With a random method of tagging adipose marrow voxels, percentage of trabeculae perimeter coverage is shown to increase linearly with decreasing marrow cellularity (1 – fat fraction).
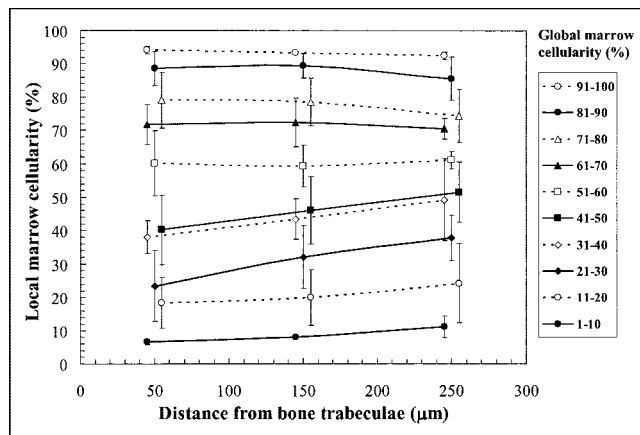

FIGURE 6. Variations in local marrow cellularity as function of both distance from bone trabeculae and global marrow cellularity of biopsy sample. Values shown are means and 1-σ errors for replicate measurements for different bone trabeculae and for up to 3 different biopsy samples. Data are plotted at means of distance intervals in staggered fashion to better display data error bars.

Figure 6 displays measurements of local marrow cellularity within 3 radial distance intervals from the bone trabeculae surface (0–100, 100–200, and 200–300 μm) as a function of the global marrow cellularity assigned to the entire biopsy ROI. No statistically significant gradients in local marrow cellularity are noted at global cellularities of >50% and <20%. For the former (fat fractions, <50%), the spatial distribution of adipocytes and their clusters appears to be uniformly distributed within the marrow cavities. For the latter (fat fractions, >80%), the density of adipose tissue is sufficiently high to conceal any gradient in adipocyte spatial position in the marrow cavities. Nevertheless, at intermediate values of global cellularity (20%–50%), the data are suggestive of a gradient in local cellularity as mean values in the first radial interval (0–100 μm) are statistically smaller than mean values in the third radial interval (200–300 μm) ($P < 0.05$). In this range of global cellularity, it appears that adipocytes are modestly localized preferentially toward the trabecular surfaces and less so within the interior regions of the marrow cavities. These observations are reasonably consistent with both the data of Figure 5 (which shows that the formation of the first fat layer nears completion at a global cellularity of ~45%) and the data of Allen et al. (*12*) on adipocyte spatial positioning in the marrow spaces of the human rib.

Electron Sources in Active Marrow

Transport simulations in 2 different NMR microscopy voxel models of trabecular bone were conducted to determine the degree to which the method of marrow voxel tagging would impact values of absorbed fraction to active marrow. Results are shown in Figures 7A and 7B for electron sources emitted in the active marrow of the femoral head of the 51-y-old man and 82-y-old woman, respec-
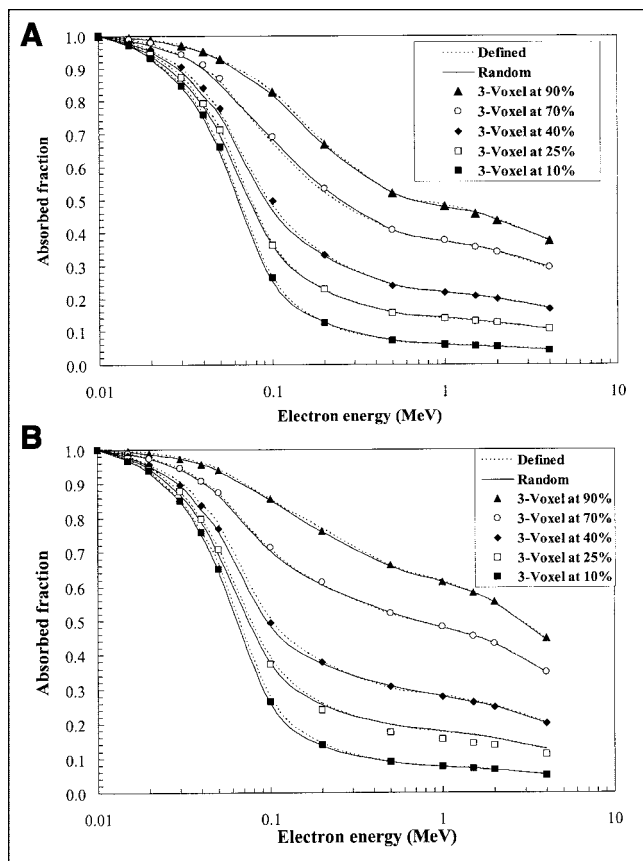
FIGURE 7. Comparison of electron absorbed fraction data, φ(TAM←TAM), for self-irradiation of TAM within femoral head of 51-y-old man (A) and that of 82-y-old woman (B). At each value of marrow cellularity, simulation results are shown for all 3 methods of adipocyte introduction within marrow cavities of 3D NMR image: DEFINED method (dashed curves), RANDOM method (solid curves), and 3-Voxel method used previously by Bolch et al. (*9*) (data symbols).

tively. Data points display values of the absorbed fraction at 5 values of marrow cellularities as taken from Bolch et al. (*9*) using the 3-Voxel method of defining the TIM. Shown in comparison are absorbed fraction data for transport simulations in which the TIM is modeled using either the DEFINED method or the RANDOM method of voxel tagging. At energies of >500 keV, all 3 methods yield essentially identical results, with the single exception of 25% marrow cellularity in the female femoral head. At energies below ~200 keV, the DEFINED method generally yields absorbed fraction values ~2%–5% higher than those calculated under the 3-Voxel or RANDOM method of adipose voxel tagging. Only at these low-emission energies would slight differences in target and nontarget geometries influence patterns of energy deposition. Comparisons of voxel-based assessments of φ(TAM←TAM) with those given by chord-based models were given previously in Bolch et al. (*9*) and have resulted in revisions to the Eckerman and Stabin model for marrow sources (*14*).

Electron Sources in TBV

When the electron emissions in trabecular bone are uniformly distributed within the volumes of the bone trabeculae, the absorbed fraction of energy to active marrow, φ(TAM←TBV), is shown to have an energy dependence as displayed in Figure 8. Figures 8A and 8B give results using the DEFINED method of adipose voxel tagging for the 51-y-old male femoral head and humeral epiphysis, respectively. Corresponding data for these same skeletal sites in the 82-y-old woman are shown in Figures 8C and 8D, respectively. In each voxel model, the marrow cellularity is allowed to vary from 25% (the ICRP reference value) to 100% as indicated. For each case, the electron emission energy must exceed ~30–40 keV for a meaningful fraction of the particles to escape the bone trabeculae, penetrate the 10-μm endosteal layer, and deposit their residual energy to voxels denoting hematopoietically active regions of the marrow tissues. At energies exceeding ~600 keV, the absorbed fraction profiles begin to decrease as electrons escape the trabecular spongiosa and deposit their residual energy to the surrounding cortex of cortical bone. For the male subject, maximum values of absorbed fraction to active marrow are noted to be higher in the humerus than in the femoral head, primarily because of the higher marrow volume fraction in the former (0.84 vs. 0.63) with its resulting thinner trabeculae (spongiosa volumes are both ~65 cm³). These same upward shifts in absorbed fraction are seen in the female subject for these 2 bone sites, although they are less dramatic.

Electron Sources in TBE and on TBS

Other bone-seeking radiopharmaceuticals localize not within the volumes of the trabeculae but at the surfaces of the bone–marrow interface. Here, one can consider the localization to occur either (a) uniformly within the 10-μm TBE (e.g., cellular incorporation within the osteoblasts) or (b) on the TBS (e.g., interface between of the mineral bone and endosteal layer). Figures 9A–9D show values of both φ(TAM←TBE) and φ(TAM←TBS) at 4 values of marrow cellularity for humerus and femoral head of both the 51-y-old-old male and the 82-y-old female subject as indicated in each panel. In the energy range of 10–40 keV, values of φ(TAM←TBE) steadily increase as more electron energy escapes from the endosteal layer to irradiate regions of the active marrow on the emission side of the bone trabeculae. As the electron emission energy increases further to ~40–100 keV, a second upturn in φ(TAM←TBE) is noted. Here, electrons emitted toward the interior of a bone trabecula now have sufficient energy to penetrate the trabecula and endosteal layer and, thus, emerge on its far side to irradiate additional voxels of active marrow. At energies exceeding several hundred keV, values of φ(TAM←TBE) merge with corresponding values of φ(TAM←TBV) as the energy distribution patterns become independent of the emission site in bone.
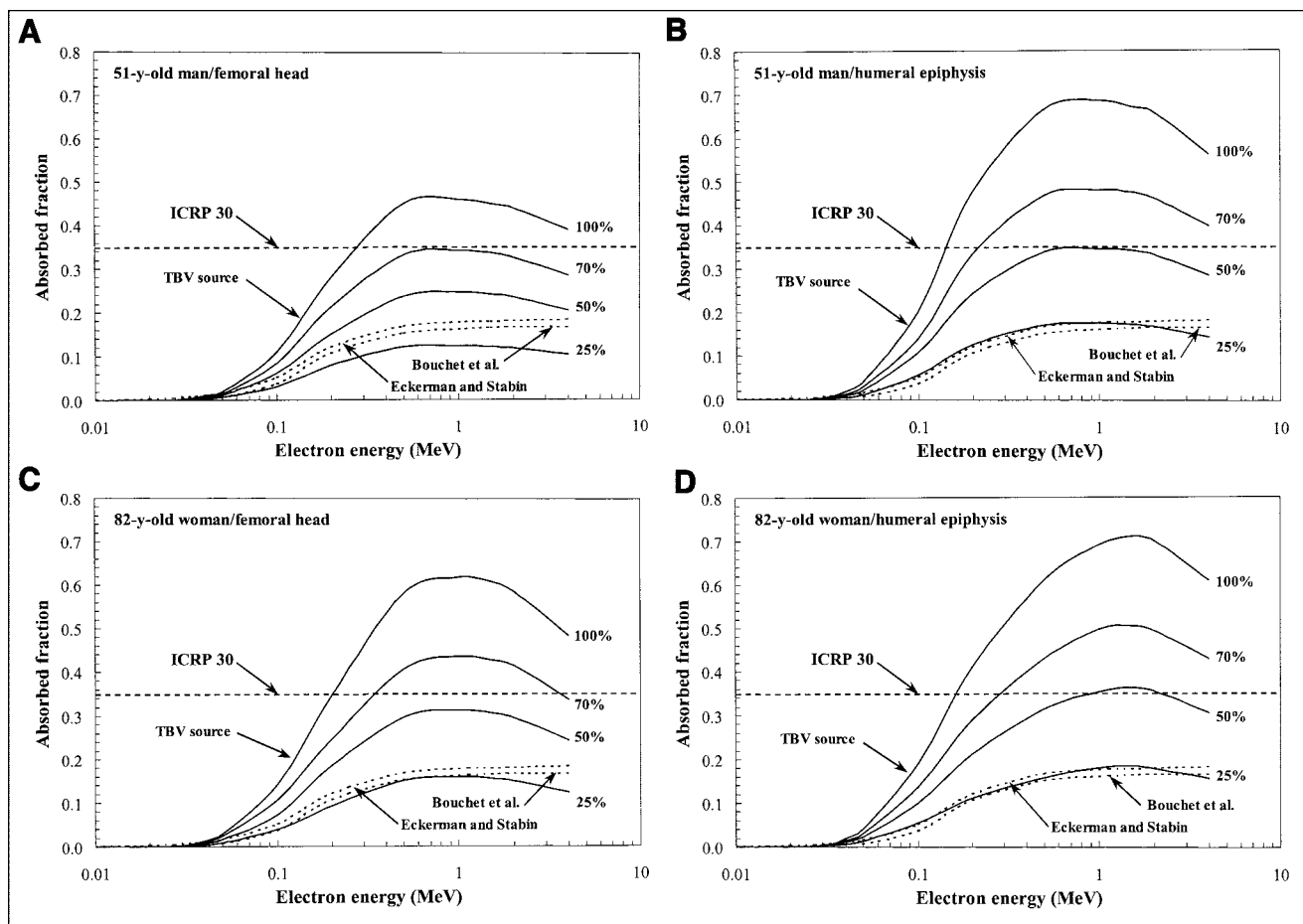
FIGURE 8. Absorbed fractions to TAM, $\phi(TAM \leftarrow TBV)$, for electron sources emitted uniformly within TBV at 4 values of marrow cellularity: 100%, 70%, 50%, and 25%. Data are shown for 2 skeletal sites and 2 individuals as indicated in A–D. For comparison, values are shown as well for ICRP 30 model (energy-independent dashed line) and both the Eckerman and Stabin (*16*) and the Bouchet et al. (*17*) models (energy-dependent dashed line).

Corresponding values of $\phi(TAM \leftarrow TBS)$ are shown in Figures 9A–9D as dashed lines which merge with values of $\phi(TAM \leftarrow TBE)$ at energies of >500 keV. For electron source energies of <100 keV, the choice of a TBE or TBS source strongly influences values of absorbed fraction to active marrow. For emissions on the TBS, the electron emission energy must exceed ~20 keV for a meaningful fraction of the particles to penetrate the 10-μm endosteal layer and deposit their residual energy to tissues of the active marrow. As with the TBE sources, a second upturn is at emission energies of 40–100 keV as particles begin to penetrate the bone trabeculae and irradiate other regions of active marrow.

DISCUSSION

Comparisons can be made between the cellularity-dependent voxel-based transport models developed in this study and 3 published models: the ICRP 30 model (*15*), the Eckerman and Stabin model (*16*), and the Bouchet et al. model (*17*). These models are based on chord-length distributions measured at the University of Leeds on a 44-y-old

male subject (*18–20*). In the latter 2 models, values of absorbed fraction to the marrow spaces determined via transport simulations have been scaled by a reference cellularity of 25% as given by the ICRP (*21*).

In Figures 8A–8D, the ICRP 30 model specifies an energy-independent value of 0.35 for all skeletal sites in Reference Man, with no consideration of marrow cellularity. In comparison with the voxel-based transport models, the absorbed fraction to active marrow is significantly overestimated by the ICRP-30 model for low-energy emitters (<300 keV) across all values of marrow cellularity. At energies of >300 keV, this energy-independent model provides a rough approximation of $\phi(TAM \leftarrow TBV)$ only at marrow cellularities of ~50%–70%.

In contrast, the cellularity-scaled models of Eckerman and Stabin and of Bouchet et al. show excellent agreement with values of $\phi(TAM \leftarrow TBV)$ from the voxel-based transport model at the same reference marrow cellularity (25%). Exceptions are noted for (a) the male femoral head, where the chord-based models yield absorbed fractions ~20%–50% higher than those given by the voxel-based model (e.g.,
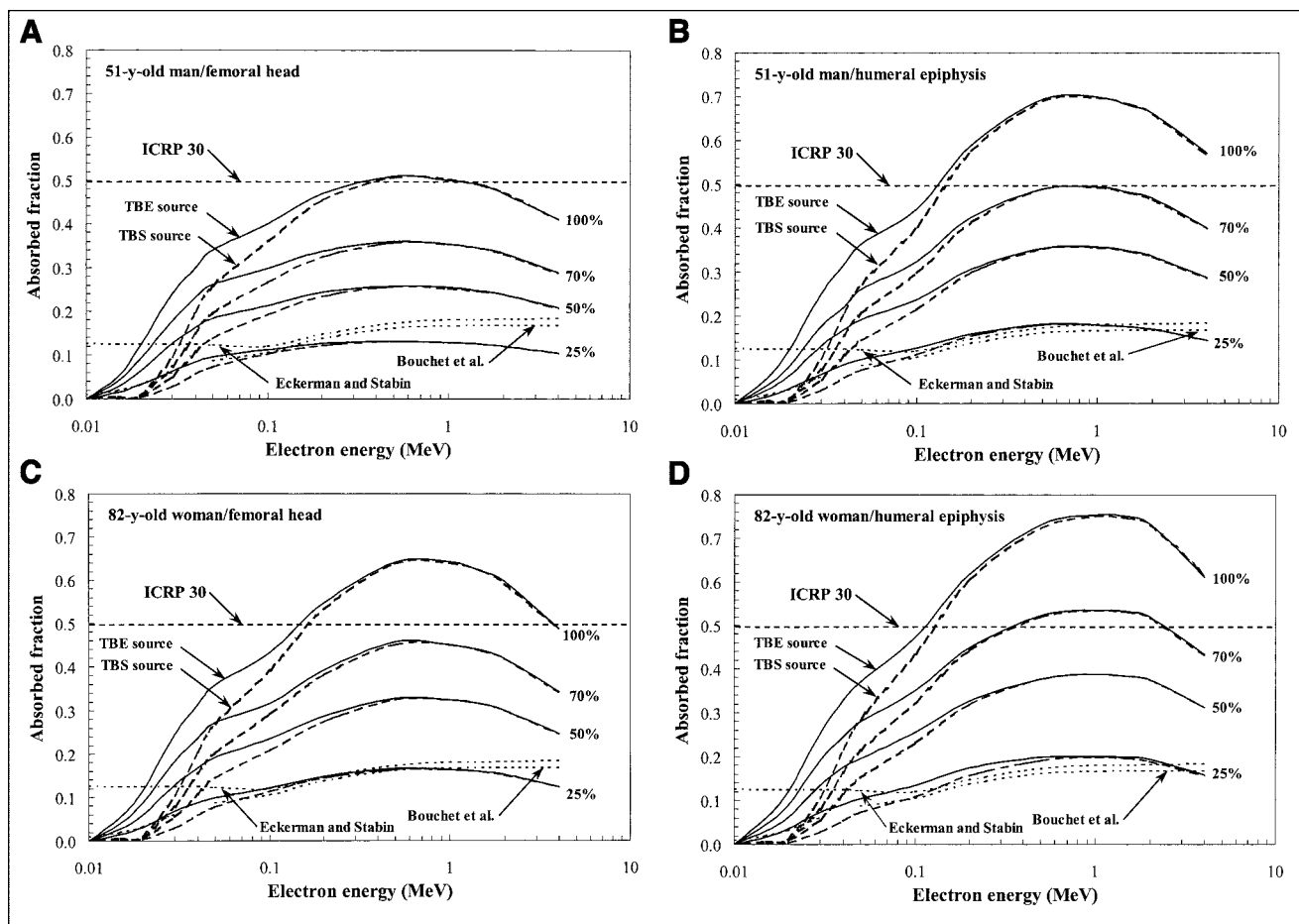
FIGURE 9. Absorbed fractions to TAM for electron sources emitted uniformly within either TBE or TBS at 4 values of marrow cellularity: 100%, 70%, 50%, and 25%. Data are shown for 2 skeletal sites and 2 individuals as indicated in A–D. For comparison, values are shown as well for ICRP 30 model (energy-independent dashed line) and both the Eckerman and Stabin (*16*) and the Bouchet et al. (*17*) models (energy-dependent dashed line).

possibly thinner trabeculae in the Leeds subject); and (b) electron emission energies exceeding ~1 MeV, where particle escape from the skeletal site is not accounted for within the chord-based models (e.g., infinite trabecular region transport as discussed in Patton et al. (*13*) and in Jokisch et al. (*22*)).

Reference values of ϕ(TAM←TBS) are shown in Figures 9A–9D from all 3 chord-based models for electron sources on the bone surfaces. In the ICRP 30 model, a simple half-space is implied in which only 50% of isotropic particle emissions reach the marrow space, where full energy deposition to active marrow is then assumed. As with the TBV sources, the ICRP 30 value of 0.50 is noted to be exceedingly conservative except in the case of high-energy emitters (>100 keV) in the humeri (Figs. 9B and 9D) and female femoral head (Fig. 9C) at high values of marrow cellularity (70%–100%).

In contrast, values of ϕ(TAM←TBS) given by the Eckerman and Stabin and the Bouchet et al. models show good to excellent agreement with voxel-model transport results at

energies of >100 keV. Discrepancies are noted, however, for electron emitters below ~100 keV for the Eckerman and Stabin model. At these energies, the Eckerman and Stabin model shows little-to-no energy dependence, as energy deposition events to the trabecular endosteum are not differentiated from those to the surrounding active marrow. Consequently, their absorbed fractions at low energies begin at 0.125 (an absorbed fraction of 0.50 multiplied by the reference marrow cellularity of 25%). In the voxel-based transport models, electron emissions on the TBS must penetrate either the 10-μm endosteal layer or adipose voxels of the first fat layer before they can participate in energy deposition to the hematopoietically active marrow.

Both the voxel-based and chord-based models discussed above are constructed using an extremely limited number of subjects; nevertheless, the voxel-based modeling data shown above tend to support the use of cellularity-scaled chord-based models from either Eckerman and Stabin (*16*) (electrons of >100 keV) or from Bouchet et al. (*17*) (all energies). Further research is needed, however, to quantify

the full extent to which individual variability in bone mineral density (e.g., bone trabeculae thicknesses) can influence dose to active marrow.

In addition to their ability to incorporate changes in marrow cellularity and skeletal site size, voxel-based skeletal dosimetry models provide the potential for reporting (a) dose–volume histograms of active marrow dose and (b) active marrow dose as a function of distance from the bone–marrow interface (23). These capabilities are not available to chord-based dose models. In voxel-based models, cellularity-dependent patterns of adipocyte clustering, trabeculae surface coverage, and adipocyte concentration gradients reported here could potentially play key roles in altering dose gradients for bone–volume and bone–surface sources. Finally, quantification of these dose gradients for various radionuclides, coupled with a knowledge of stem and progenitor cell concentrations within the marrow cavities (24), might provide an improved basis for predicting marrow response in radionuclide therapies.

CONCLUSION

Experimental data have been collected on the spatial distributions of adipocytes in normal human bone marrow as needed to define the inactive (yellow) marrow regions in 3D voxel models of trabecular bone. These studies included measurements of (a) size distributions of adipocyte cell clusters, (b) the fractional perimeter coverage of bone trabeculae perimeter by marrow adipocytes, and (c) the presence or absence of cellularity gradients within the marrow cavity. Study 1 revealed a predicable shift in cluster size with decreasing marrow cellularity from single adipocytes to clusters of ≥3 cells; the percentage of 2-cell clusters remained relatively constant with changing cellularity. Study 2 revealed a small nonlinear variation in trabeculae perimeter coverage with increasing fat tissue fraction at marrow cellularities between 50% and 80%. Study 3 demonstrated that only in the range of 20%–50% marrow cellularity was a slight gradient in adipocyte concentration indicated with adipocytes localized preferentially toward the trabecular surfaces. These data were subsequently used to assemble 3D images of trabecular bone with both active (red) and inactive (yellow) marrow delineated in patterns consistent with the marrow biopsy measurements. As demonstrated in Figure 7, however, electron dosimetry of the skeletal site remains fairly independent of the method by which adipocyte clusters are introduced. At image resolutions of ~88 μm, the 3-Voxel and RANDOM methods provide reasonable alternatives to the DEFINED method of adipocyte spatial characterization in the 3D images.

For both bone volume and bone surface electron sources, absorbed fractions to active marrow given by the ICRP 30 model (MIRDOSE2) were shown to be exceedingly conservative except in the case of high-energy emissions (>500 keV) and at high values of marrow cellularity (>70%). Values of both $\phi(TAM \leftarrow TBV)$ and $\phi(TAM \leftarrow TBS)$ given by the Eckerman and Stabin model (MIRDOSE3) were shown to be reasonably consistent with 3D voxel model simulations at the reference cellularity of 25%, except in the case of low-energy emitters (<100 keV) on the bone surfaces. The data of Figures 8 and 9 further highlighted the need for careful specification of skeletal source location for those bone-seeking radiopharmaceuticals with low-energy particles (<100 keV) in their emission spectrum, as estimates of absorbed fraction to active marrow can vary greatly at these energies.

REFERENCES

1. Sgouros G. Bone marrow dosimetry for radioimmunotherapy: theoretical considerations. *J Nucl Med.* 1993;34:689–694.
2. Sgouros G, Jureidini IM, Scott AM, Graham MC, Larson SM, Scheinberg DA. Bone marrow dosimetry: regional variability of marrow-localizing antibody. *J Nucl Med.* 1996;37:695–698.
3. Siegel JA, Pawlyk DA, Lee RE, et al. Tumor, red marrow, and organ dosimetry for ^{131}I-labeled anti-carcinoembryonic antigen monoclonal antibody. *Cancer Res.* 1990;50(3 suppl):1039s–1042s.
4. Siegel JA, Lee RE, Pawlyk DA, Horowitz JA, Sharkey RM, Goldenberg DM. Sacral scintigraphy for bone marrow dosimetry in radioimmunotherapy. *Int J Rad Appl Instrum B.* 1989;16:553–559.
5. Juweid M, Sharkey RM, Siegel JA, Behr T, Goldenberg DM. Estimates of red marrow dose by sacral scintigraphy in radioimmunotherapy patients having non-Hodgkin's lymphoma and diffuse bone marrow uptake. *Cancer Res.* 1995;55(23 suppl):5827s–5831s.
6. Macey DJ, DeNardo SJ, DeNardo GL, DeNardo DA, Shen S. Estimation of radiation absorbed doses to the red marrow in radioimmunotherapy. *Clin Nucl Med.* 1995;20:117–125.
7. Ballon D, Jakubowski AA, Graham MC, Schneider E, Koutcher JA. Spatial mapping of the percentage cellularity in human bone marrow using magnetic resonance imaging. *Med Phys.* 1996;23:243–250.
8. Ballon D, Jakubowski AA, Tulipano PK, et al. Quantitative assessment of bone marrow hematopoiesis using parametric magnetic resonance imaging. *Magn Reson Med.* 1998;39:789–800.
9. Bolch WE, Patton PW, Rajon DA, Shah AP, Jokisch DW, Inglis B. Considerations of marrow cellularity in 3-dimensional dosimetric models of the trabecular skeleton. *J Nucl Med.* 2002;43:97–108.
10. Rozman C, Feliu E, Berga L, Reverter JC, Climent C, Ferran MJ. Age-related variations of fat tissue fraction in normal human bone marrow depend both on size and number of adipocytes: a stereological study. *Exp Hematol.* 1989;17:34–37.
11. Rozman C, Reverter JC, Feliu E, Berga L, Rozman M, Climent C. Variations of fat tissue fraction in abnormal human bone marrow depend both on size and number of adipocytes: a stereologic study. *Blood.* 1990;76:892–895.
12. Allen JE, Henshaw DL, Keitch PA, Fews AP, Eatough JP. Fat cells in red bone marrow of human rib: their size and spatial distribution with respect to the radon-derived dose to the haemopoietic tissue. *Int J Radiat Biol.* 1995;68:669–678.
13. Patton PW, Rajon DA, Shah AP, Jokisch DW, Inglis B, Bolch WE. Site-specific variability in trabecular bone dosimetry: considerations of energy loss to cortical bone. *Med Phys.* 2002;29:6–14.
14. Stabin MG, Eckerman KF, Bolch WE, Bouchet LG, Patton PW. Evolution and

status of bone and marrow dose models. *Cancer Biother Radiopharm.* 2002;17:427–445.

15. ICRP. *Limits for Intakes of Radionuclides by Workers.* ICRP Publication 30. Oxford, U.K.: International Commission on Radiological Protection; 1979.

16. Eckerman KF, Stabin MG. Electron absorbed fractions and dose conversion factors for marrow and bone by skeletal regions. *Health Phys.* 2000;78:199–214.

17. Bouchet LG, Jokisch DW, Bolch WE. A three-dimensional transport model for determining absorbed fractions of energy for electrons in trabecular bone. *J Nucl Med.* 1999;40:1947–1966.

18. Whitwell JR. *Theoretical Investigations of Energy Loss by Ionizing Particles in Bone* [thesis]. Leeds, U.K.: Department of Medical Physics, University of Leeds; 1973.

19. Whitwell JR, Spiers FW. Calculated beta-ray dose factors for trabecular bone. *Phys Med Biol.* 1976;21:16–38.

20. Beddoe AH, Darley PJ, Spiers FW. Measurements of trabecular bone structure in man. *Phys Med Biol.* 1976;21:589–607.

21. ICRP. *Basic Anatomical and Physiological Data for Use in Radiological Protection: The Skeleton.* ICRP Publication 70. Oxford, U.K.: International Commission on Radiological Protection; 1995.

22. Jokisch DW, Bouchet LG, Patton PW, Rajon DA, Bolch WE. Beta-particle dosimetry of the trabecular skeleton using Monte Carlo transport within 3D digital images. *Med Phys.* 2001;28:1505–1518.

23. Kvinnsland Y, Skretting A, Bruland OS. Radionuclide therapy with bone-seeking compounds: Monte Carlo calculations of dose-volume histograms for bone marrow in trabecular bone. *Phys Med Biol.* 2001;46:1149–1161.

24. Lord BI. The architecture of bone marrow cell populations. *Int J Cell Cloning.* 1990;8:317–331.